



Cracking potential of alkali-activated slag and fly ash concrete subjected to restrained autogenous shrinkage

Zhenming Li^{a,*}, Shizhe Zhang^a, Xuhui Liang^a, Guang Ye^{a,b}

^a Department of Materials and Environment (Microlab), Faculty of Civil Engineering and Geoscience, Delft University of Technology, Delft, the Netherlands

^b Magne Laboratory for Concrete Research, Department of Structural Engineering, Ghent University, Ghent, Belgium

ARTICLE INFO

Keywords:

Cracking
Shrinkage
Stress
Alkali-activated materials
Concrete
Modelling

ABSTRACT

This study aims to investigate the cracking potential of alkali-activated slag (AAS) and alkali-activated slag-fly ash (AASF) concrete subjected to restrained autogenous shrinkage. Temperature Stress Testing Machine (TSTM) is utilized, for the first time, to monitor the stress evolution and to measure the cracking time of alkali-activated concrete (AAC) under restraint condition. The stresses in AAS and AASF concrete are calculated based on the experimental results while taking into consideration the influence brought by creep and relaxation. It is found that AAS and AASF concrete showed lower autogenous shrinkage-induced stress and later cracking compared to ordinary Portland cement (OPC) based concrete with similar compressive strength, despite the higher autogenous shrinkage of AAS and AASF concrete. The low autogenous shrinkage-induced stress in the AAC is mainly attributed to the pronounced stress relaxation. A good prediction of the stress evolution in AAC is obtained by taking into account the elastic part of the autogenous shrinkage and the stress relaxation. In contrast, calculations ignoring the creep and relaxation would lead to a significant overestimation of the stress in AAC.

1. Introduction

Alkali-activated materials (AAMs) have emerged as eco-friendly alternatives to OPC as binder materials in engineering practice [1]. In comparison to OPC, AAMs can significantly reduce the environmental impacts of concrete products by lowering greenhouse gas emissions and the embodied energy [2]. Furthermore, using AAMs as binders could also contribute to the repurposing of industrial by-products [3,4].

Currently, granulated blast-furnace slag (hereinafter termed slag) and powered coal fly ash (hereinafter termed fly ash) are the two most widely utilized precursors for AAMs. Among two types of fly ash, namely Class C and Class F fly ash according to ASTM C618 [5], Class F fly ash with reactive $\text{CaO} \leq 10\%$ has been intensively studied worldwide due to its wide availability and high content of amorphous aluminosilicate phases [6]. Alkali activator is usually an alkali metal hydroxide and/or silicate [7]. Although Na_2CO_3 and Na_2SO_4 can also be used as activators [8,9], the majority of studies have shown that activation with Na_2SiO_3 and/or NaOH provides high mechanical properties for slag and fly ash-based AAMs [10]. NaOH activators are found to accelerate early-age activation but tend to present a barrier to advanced reactions, therefore limiting the later-age strength [11]. In contrast, the reaction of

Na_2SiO_3 -activated slag is comparatively slow and results in the formation of very dense products with improved mechanical strength [12].

Despite the promising mechanical and eco-friendly performance, slag and fly ash-based AAMs have not received broad industry acceptance, primarily due to the uncertain long-term durability and volume stability [13–15]. As reported in Ref. [16–24,76], slag and fly ash-based AAMs, especially those activated by NaOH/ Na_2SiO_3 , can show higher autogenous shrinkage than common OPC based systems. The high autogenous shrinkage of AAMs is concerned by both academia and industrial communities because it can potentially induce cracking of concrete [25,26]. In practice, concrete as building material is normally applied under restrained conditions. The restraint can be either external (e.g. caused by adjoining structure) or internal (e.g., caused by the reinforcement or the non-shrinking aggregates) to the concrete member [27–29]. The volume change of the concrete would be therefore limited to a certain extent and consequently internal tensile stress would develop. Cracking would occur when the tensile stress within concrete exceeds the tensile strength, which can lead to a series of problems regarding mechanical properties, durability and aesthetics of concrete structures [30]. Therefore, the cracking potential of activated slag and fly ash concrete has to be evaluated to provide a solid theoretical basis

* Corresponding author.

E-mail address: z.li-2@tudelft.nl (Z. Li).

<https://doi.org/10.1016/j.cemconcomp.2020.103767>

Received 2 March 2020; Received in revised form 24 July 2020; Accepted 29 July 2020

Available online 17 August 2020

0958-9465/© 2020 The Authors. Published by Elsevier Ltd. This is an open access article under the CC BY license (<http://creativecommons.org/licenses/by/4.0/>).

for safe and reliable application of these materials.

From the high autogenous shrinkage of alkali-activated slag and fly ash systems, one may deduce that AAC will show higher cracking potential compared to OPC based concrete. However, the cracking potential of concrete is determined not only by autogenous shrinkage but also by elastic modulus, creep/relaxation and tensile strength of the material. However, very few studies on this topic can be found from the literature [31].

The aim of this study, therefore, is to evaluate the autogenous shrinkage-induced cracking potential of AAS and AASF concrete. Temperature Stress Testing Machine (TSTM) is utilized to track the internal stress evolution and cracking initiation of the concrete under restraint condition. With the measured autogenous shrinkage and elastic modulus as inputs, the internal stresses in AAS and AASF concrete are calculated and compared with the experimental results. The roles of creep and relaxation in influencing the stress evolution and cracking potential of AAC are highlighted.

2. Materials and methods

2.1. Raw materials and mixtures

The precursors used were slag supplied by Ecocem Benelux B.V and fly ash from Vliegassunie B.V. The chemical compositions of slag and fly ash were determined by X-ray fluorescence (XRF) and shown in Table 1. The fly ash complies with Class F (EN 450, ASTM C618) since it has low CaO content (<10% reactive CaO) and content of “SiO₂ + Al₂O₃ + Fe₂O₃” higher than 70%. The particle size of slag, as measured by laser diffraction, ranges from 0.1 to 50 µm, with a d₅₀ of 18.3 µm. The particle size of fly ash is between 0.14 and 138 µm, with a d₅₀ of 48.1 µm.

The alkaline activator was prepared by mixing anhydrous pellets of sodium hydroxide with deionized water and commercial sodium silicate solution. For 1000 g of precursor, an activator containing 384 g of water, 1.146 mol of SiO₂ and 0.76 mol of Na₂O was applied. The water-to-solid ratio is therefore 0.344 if the alkali in the activator is considered as solid. The activator was prepared at least one day before the casting of the concrete so that the solution was cooled down to ambient temperature.

The concrete mixture designs are shown in Table 2.

2.2. Experimental methods

2.2.1. Mechanical properties

Concrete cubes (150 × 150 × 150 mm³) for compressive and splitting strength tests and prisms (100 × 100 × 400 mm³) for elastic modulus test were cast and cured in sealed and temperature-controlled steel moulds. The moulds were connected with cryostats by parallel circulation tubes and the upper surface was sealed by plastic film. The temperature of the concrete cubes was controlled at 20 °C.

Compressive strength and splitting strength of the concrete were measured according to NEN-EN 12390 [32]. The measurements were conducted at the age of 1, 3, 7, 28 days and the day when the beam in TSTM cracked. One cube was tested for compressive strength and two for splitting strength.

The elastic modulus of the concrete was tested by a Tonibank hydraulic Instron (Fig. 1). The strain during loading was measured by linear variable differential transducers (LVDTs) aligned vertically on the four sides of the concrete prism. The loading and unloading of each sample went through four cycles with the stress ranging from 5% to 30%

Table 1

Chemical propositions of slag and fly ash.

Oxide (wt. %)	SiO ₂	Al ₂ O ₃	CaO	MgO	Fe ₂ O ₃	SO ₃	K ₂ O	TiO ₂	Other	LOI
Slag	31.77	13.25	40.50	9.27	0.52	1.49	0.34	0.97	0.21	1.31
Fly ash	56.8	23.8	4.8	1.5	7.2	0.3	1.6	1.2	1.6	1.2

LOI = Loss on ignition.

Table 2

Mixture design of AAS and AASF concrete (kg/m³).

Mixtures	AAS	AASF
Slag	400	200
Fly ash	0	200
Activator	200	200
Aggregate [0–4 mm]	789	789
Aggregate [4–8 mm]	440	440
Aggregate [8–16 mm]	525	525
Admixtures	–	–



Fig. 1. Testing set-up for elastic modulus measurement on AAC.

of the compressive strength of the concrete. The results obtained from the latter three cycles were used in the calculation of the elastic modulus. The loading and unloading rates were 1 kN/s [33]. Two samples were tested for each mixture at each age.

2.2.2. Autogenous shrinkage

The autogenous shrinkage of the concrete was measured with an Autogenous Deformation Testing Machine (ADTM) [34]. The prismatic mould for the concrete is made of thin steel plates and external insulating materials. The size of the mould is 1000 × 150 × 100 mm³, which is illustrated in Fig. 2. The mould was connected with cryostats by a series of circulation tubes located between the plates and the insulating material (see Fig. 2). The temperature of the beam was controlled at 20 °C.

The length change of the concrete was measured with two external quartz rods located next to the side mould. LVDTs were installed at both ends of the rods. The LVDTs measured the movement of the steel bars which were cast in the concrete. The distance between the two cast-in

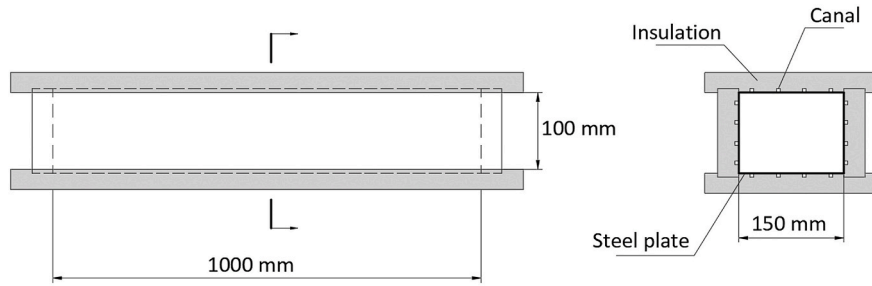


Fig. 2. Front view (left) and cutaway view (right) of the mould of Autogenous Deformation Testing Machine (ADTM).

steel bars was 750 mm. The instalment of LVDTs was conducted only when the concrete had reached sufficient strength to support them (see Fig. 3). The measurement of the deformation of AAS and AASF concrete starts at 8 h and 11 h, respectively. Attention was paid to the sealing of the moulds in order to avoid moisture loss to the environment.

2.2.3. Autogenous shrinkage-induced stress

The internal tensile stress in the concrete induced by restrained autogenous shrinkage was monitored by TSTM. A sudden drop of the stress indicated the occurrence of cracking. The TSTM was equipped with a horizontal steel frame (Fig. 4) in which the concrete specimen can be loaded in compression or in tension under various temperatures. The whole specimen is of a dog-bone shape and the testing area of interest is of prismatic shape ($1000 \times 150 \times 100 \text{ mm}^3$). The middle part of the specimen is in a temperature-controlled mould, similar to the ADTM mould as described in Section 2.2.2. Two rigid steel claws were used to grip the concrete specimen. One of the claws was fixed to the steel frame while the other one lied on roller bearings and thereby can move with the hydraulic actuator to provide a compressive or tensile force onto the testing specimen. A short formwork was attached to the claws to provide a smooth and curved transition between the straight insulated mould and the slanting inner sides of the claws. The load was recorded with the load-cell with a loading capacity of 100 kN and a resolution of 0.049 kN.

During the first 8 h after casting, LVDTs were used to control the deformation between the two claws because it was not yet possible to measure the deformations of the fresh concrete with the embedded steel bars. After that, the deformation control was switched to the LVDTs that measure the displacement between the embedded bars. The deformation of the concrete was kept at zero (nominally, in reality within $1 \mu\text{m}$ range) so that a full restraint condition was provided.

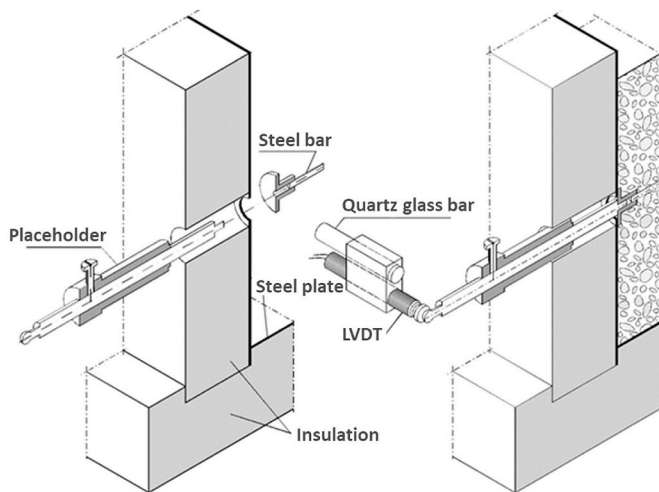


Fig. 3. Installation of measuring bars and placeholders before casting (left) and installation of LVDTs when the concrete is stiff enough to support the bars (right), after [34].

2.3. Calculation of the autogenous shrinkage-induced stress

While the autogenous shrinkage-induced stress in restrained concrete can be monitored by TSTM, the test is very time-consuming and labour-intensive. Besides, TSTM is currently not equipped widely enough to serve as a standard apparatus. Therefore, it would be meaningful if the stress evolution can be predicted based on the experimental results obtained in concrete under free conditions.

2.3.1. Calculation of the stress based on autogenous shrinkage

If the autogenous shrinkage is assumed to be purely elastic deformation [28], the stress (σ_{AS}) generated in the concrete due to restrained shrinkage can be calculated using Equation (1). A schematic representation of the calculation process is shown in Fig. 5.

$$\sigma_{AS} = \varepsilon_{AS} \times E \quad (1)$$

where ε_{AS} is the measured autogenous shrinkage of the concrete and E is the measured elastic modulus of the concrete.

2.3.2. Calculation of the stress based on the elastic part of the autogenous shrinkage

In fact, the concrete, either OPC based concrete or AAC, is not a purely elastic material [25,36]. Under external or internal load, the concrete tends to generate time-dependent deformation, or so-called creep, due to the viscoelasticity of the material. Therefore, a part of the autogenous shrinkage of the concrete measured under free condition actually belongs to creep deformation [37]. When the concrete is under externally restrained condition, the creep part of the autogenous shrinkage does not have the potential to develop due to the equilibrium between the internal driving force and the external restraint force. Therefore, the stress in the restrained concrete is predominantly caused by the elastic part of the autogenous shrinkage [38]. If we assume the stress in the concrete is solely induced by the elastic part of the autogenous shrinkage and do not consider the stress relaxation, the stress can be calculated using Equations (2) and (3). A schematic representation of the calculation process is shown in Fig. 6.

$$\varepsilon_{AS} = \varepsilon_{AS,elas} + \varepsilon_{AS,creep} \quad (2)$$

where ε_{AS} is the measured autogenous shrinkage of AAC. $\varepsilon_{AS,elas}$ and $\varepsilon_{AS,creep}$ are the elastic part and creep part of the autogenous shrinkage of AAC, respectively.

$$\sigma_{AS,elas} = \varepsilon_{AS,elas} \times E \quad (3)$$

where $\sigma_{AS,elas}$ is the stress induced by the elastic part of the autogenous shrinkage ($\varepsilon_{AS,elas}$).

The relationship between the creep deformation and the elastic deformation under a load can be expressed by Equation (4) [25,39].

$$\varepsilon_{AS,creep}(t, \tau) = \varepsilon_{AS,elas}(\tau) \phi(t, \tau) \quad (4)$$

where $\phi(t, \tau)$ is the creep coefficient. τ (days) is the time when the load is applied.

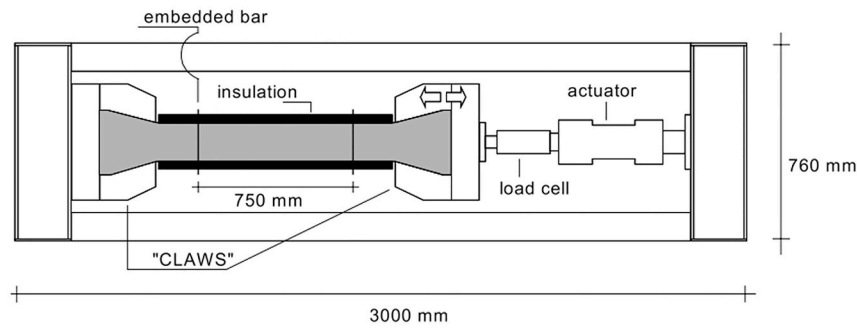


Fig. 4. Top view of the Temperature Stress Testing Machine (TSTM) [35].

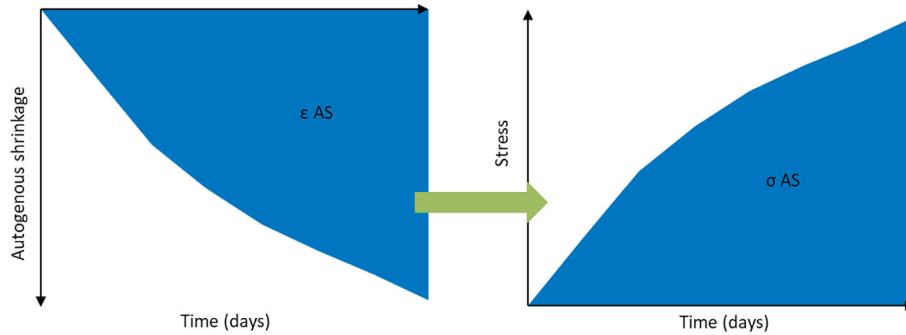


Fig. 5. Schematic representation of stress calculated based on autogenous shrinkage.

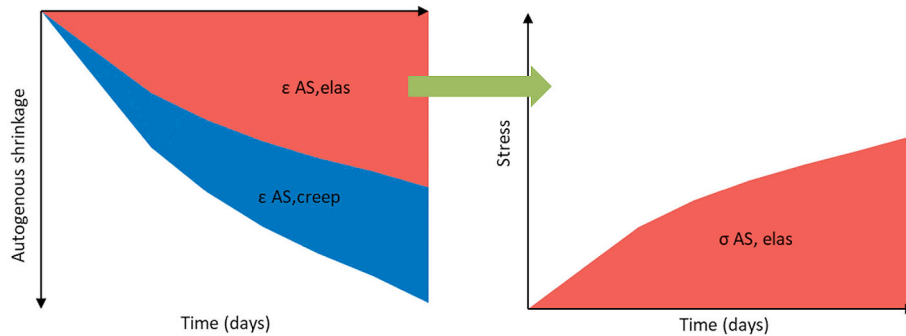


Fig. 6. Schematic representation of stress calculated based on the elastic part of the autogenous shrinkage.

According to Ref. [38,40], the creep coefficient of OPC based concrete can be calculated by Equation (5). For AAC systems, however, no models are available yet to account for the creep deformation. Therefore, Equation (5) is tentatively used in this study to calculate the creep coefficient of AAC.

$$\phi(t, \tau) = \left(\frac{\alpha(t)}{\alpha(\tau)} - 1 \right) + 1.34 * \omega^{1.65} \tau^{-d} (t - \tau)^n \frac{\alpha(t)}{\alpha(\tau)} \quad (5)$$

where α is the degree of reaction. ω is the water-to-solid ratio (0.344, see section 2.1). n is the relaxation factor whose value is empirically taken as 0.3 and d is the constant whose value is empirically taken as 0.35 according to Ref. [40].

The reaction degree α of the concrete can be calculated with Equation (6) [41–43].

$$\alpha(t) = \frac{Q(t)}{Q_{max}} \quad (6)$$

where $Q(t)$ is the reaction heat and Q_{max} is the ultimate total heat at the completion of the reaction. $Q(t)$ and Q_{max} of AAC are calculated

according to the procedure described in Appendix A.

With Equations 2 and 4–6, the elastic part and creep part of the autogenous shrinkage of AAC can be calculated.

2.3.3. Calculation of the stress by taking relaxation into account

Like the creep of the concrete under free condition, stress relaxation in concrete under restrained condition is another result of the viscoelasticity of the material. Due to the relaxation, the stress generated in restrained concrete would be reduced with the elapse of time. According to van Breugel [38], the stress induced by restrained elastic deformation can be calculated with Equation (7) by taking into consideration of the relaxation. A schematic representation of the calculation process of the stress induced by restrained autogenous shrinkage is shown in Fig. 7.

$$\sigma_{relaxed}(t, \tau) = \sigma_{elas}(\tau) \psi(t, \tau) \quad (7)$$

where $\psi(t, \tau)$ is the relaxation factor. τ (days) is the time when the load is applied.

The relaxation coefficient of concrete can be calculated from the creep coefficient $\phi(t, \tau)$ using Equation (8) [38,44].

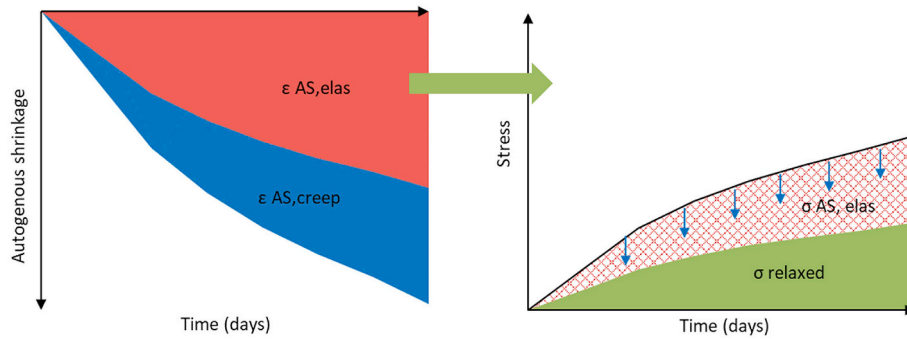


Fig. 7. Schematic representation of stress calculated based on the elastic part of the autogenous shrinkage by taking relaxation into account.

$$\psi(t, \tau) = e^{-\phi(t, \tau)} \quad (8)$$

The stress generated in the concrete after a certain curing age can be considered as the accumulations of the stresses resulting from the elastic deformations that occurred at previous time intervals, e.g. from τ_1 to τ_{n-1} , as shown in Equation (9).

$$\sigma_{relaxed} = \sum_{k=1}^{n-1} \Delta \sigma_{relaxed}(\tau_k) \quad (9)$$

where $\Delta \sigma_{relaxed}(t_k, \tau_k)$ is the increment of elastic shrinkage-induced stress after relaxation from τ_k to τ_{k+1} .

A schematic representation of the calculation process mentioned above is shown in Fig. 8.

3. Experimental results and discussion

3.1. Mechanical properties

3.1.1. Compressive and splitting tensile strength

The strength development of the concrete is shown in Fig. 9. It can be seen that AAC generally shows high strength. At the age of 28 days, the compressive strength of AAS and AASF concretes is around 90 MPa and 75 MPa, respectively. According to EN 206 [45], the strength can be classified as C60 or higher. AAS concrete shows higher compressive and splitting strength than AASF concrete, which is consistent with the findings on the positive correlation between slag/fly ash ratio and the mechanical properties in the literature [46–48]. The lower strength of AASF concrete is due to the replacement of slag by fly ash, which has a low reactivity at ambient temperature [49]. The dissolution of fly ash particles is slow no matter in cementitious systems or in alkali-activated systems [49,50]. Nonetheless, with the elapse of time the amorphous phases in fly ash would eventually contribute to the strength growth [50], which can be reflected by the considerable increase of the compressive strength of AASF concrete from 7 days to 28 days.

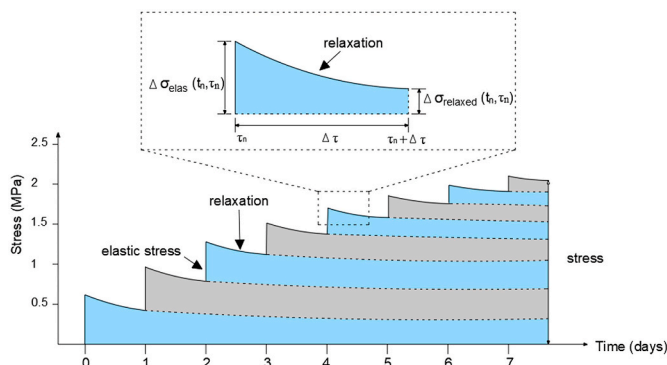


Fig. 8. Schematic representation of stress generated in concrete.

Despite the high compressive strength of AAC mixtures, their splitting tensile strength is not remarkably high. This can be seen more clearly in Fig. 10, in which the splitting tensile strength -to-compressive strength ($f_{t,sp}/f_c$) ratios of the concrete are plotted. The $f_{t,sp}/f_c$ ratio is an important parameter that allows the estimation of $f_{t,sp}$ by knowing f_c or vice versa [51]. The ratio also provides insight into the stress type (compression or tension) to which the concrete is more prone. It can be seen from Fig. 10 that AAS and AASF concretes showed nearly identical $f_{t,sp}/f_c$ except at the age of 3 days.

The $f_{t,sp}/f_c$ ratio of AAC decreases from around 0.1 at the first day to only 0.055 at 28 days. This decrease might be due to the development of microcracking within the concrete resulting from the restrained autogenous shrinkage of the material [52,53]. Although the samples for strength test were not subject to external restraint, the aggregates can act as local restraints to the autogenous shrinkage of the surrounding paste [54]. Due to the large autogenous shrinkage of AAC (as will be discussed in the following section), microcracks may have developed within the concrete, although no visual cracks were observed on the surface of the sample. The development of microcracking can harm the increase of tensile strength. Although the absolute tensile strength of AAC increased with the curing age as shown in Fig. 9, the developing rate of the tensile strength became lower than that of the compressive strength as indicated by the decreasing $f_{t,sp}/f_c$.

3.1.2. Elastic modulus

The elastic modulus of AAC is shown in Fig. 11. AAS concrete showed higher elastic modulus than AASF concrete at the early age. After 7 days, however, the elastic modulus of AAS concrete started to decrease slightly while the one of AASF concrete kept increasing. At 28 days, AAS and AASF concrete showed similar elastic modulus.

The decline of elastic modulus of AAS concrete with curing age has also been reported by Prinsse et al. [53], in which both reduced elastic modulus and splitting tensile strength were observed in AAS concrete. In that study, the concrete was cured in a climate chamber with the temperature at 20 °C and the relative humidity above 95%, after demoulded at 1 day. The reduction was attributed to the leaching of ions from the sample and the change of curing condition when the samples were taken out from the climate chamber to ambient condition for testing [53]. The loss of structural ions due to leaching and the severe drop of the environment relative humidity from above 95% to around 50% may induce substantial drying shrinkage and related microcracking, thus damaging the microstructure of the concrete [55]. This study, in contrast, applied sealed curing before the samples were tested in ambient relative humidity. Therefore, no leaching occurred. The change of the environment RH and the impact on the consequent drying shrinkage should be much less severe than that reported in Ref. [53]. However, the autogenous shrinkage, as will be discussed in the coming section, had already been developing before the exposure of the samples for strength tests, which can also induce microcracking. Therefore, the reduced elastic modulus of AAS concrete herein is believed to be due to the same reason for the reduced $f_{t,sp}/f_c$ of the concrete, which is the development of

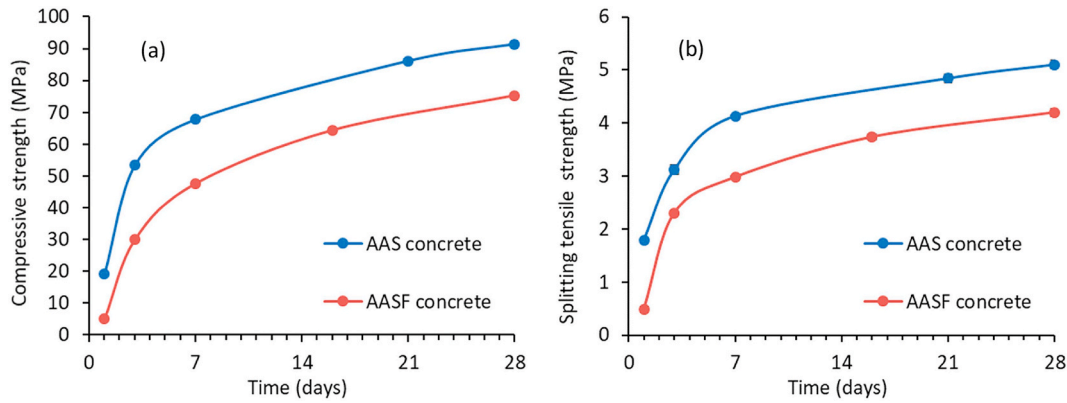


Fig. 9. Compressive (a) and splitting strength (b) of AAC. For the splitting strength, the error bar is shown in the diagram, but it is too small to be clearly distinguished from the marker.

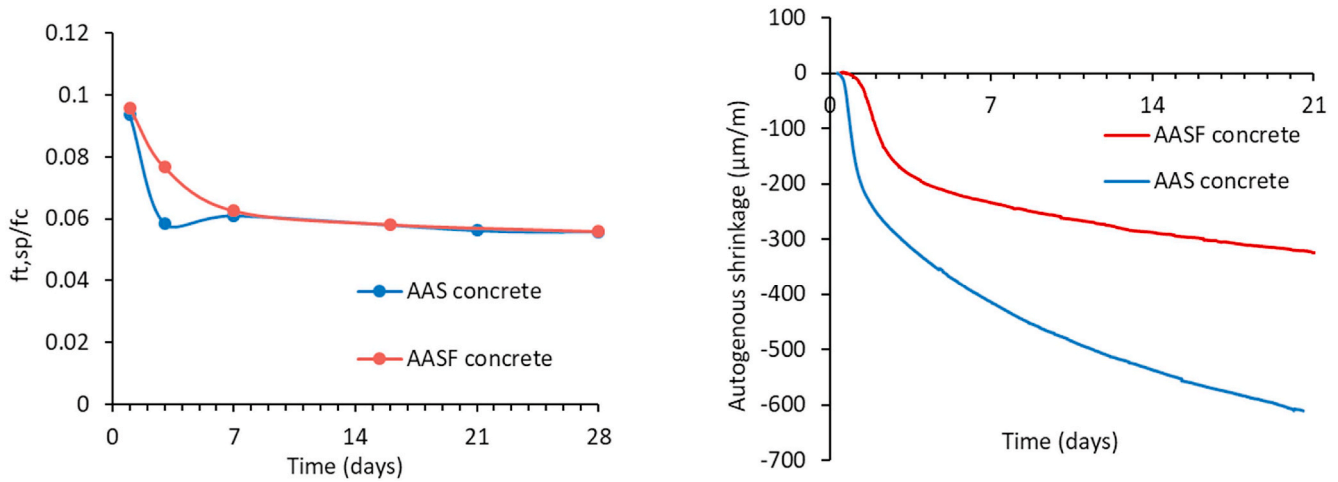


Fig. 10. Splitting tensile strength-to-compressive strength ($f_{t,sp}/f_c$) ratios of AAC.

Fig. 12. Autogenous shrinkage of AAC obtained from ADTM measurements.

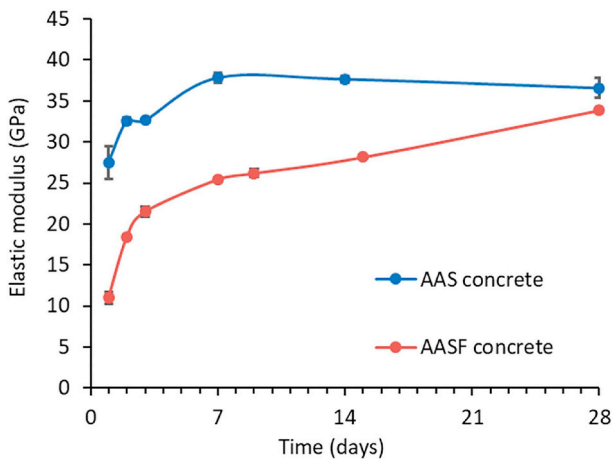


Fig. 11. Elastic modulus of AAC.

microcracking caused by autogenous shrinkage.

3.2. Autogenous shrinkage

The autogenous shrinkage of the concrete is shown in Fig. 12. AASF concrete showed lower autogenous shrinkage than AAS concrete in the whole period studied. This findings are consistent with the autogenous

shrinkage results on corresponding AAS and AASF pastes [36]. The autogenous shrinkage of AAS and AASF concrete develops rapidly at the first day and second day, respectively, which are in line with the accelerated reaction stages of the mixtures (see Fig. A.1). At the age of 21 days, the autogenous shrinkage of AAS and AASF concrete reaches 609 and 325 $\mu\text{m/m}$, respectively.

3.3. Autogenous shrinkage-induced stress

Fig. 13 shows the stress development in AAS and AASF concrete tested by TSTM. The sudden drop in the stress to around zero indicates the occurrence of cracking in concrete. It can be seen that AAS concrete showed a rapid stress development due to the high autogenous shrinkage. The stress in AASF concrete remains low in the first 1.5 days due to low shrinkage (see Fig. 12). The tensile stress generated in AASF concrete was substantially lower than in AAS concrete. The lower autogenous shrinkage and also the lower elastic modulus of AASF concrete contribute to the lower stress in AASF concrete than in AAS concrete. Nonetheless, the tensile strength (1.4 MPa) tested by TSTM of AASF concrete was also lower than that of AAS concrete (2.7 MPa). Eventually, AASF concrete cracked even earlier than AAS concrete.

The classification of cracking potential according to ASTM C1581 [35] is shown in Table 3, where cracking time (in days) and average stress rate (in MPa/day) were considered. Accordingly, the cracking potential of the two concrete mixtures belongs to the category “moderate-low”. Compared with the results obtained by TSTM on OPC based concrete in the literature [30,56,57], it can be seen that AAC showed lower stress and later cracking than OPC based concrete with similar

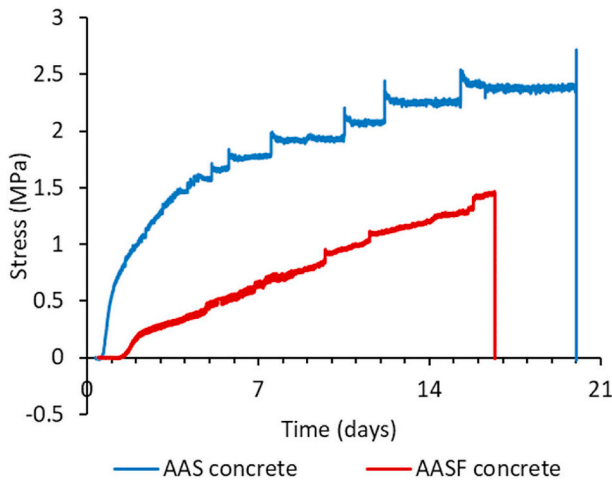


Fig. 13. Autogenous shrinkage-induced stress in AAC obtained by TSTM measurements.

Table 3

Classification of cracking potential according to ASTM C1581 [35].

Cracking time t_{cr} (days)	Average stress rate S (MPa/day)	Potential for cracking
$0 < t_{cr} \leq 7$	$S \geq 0.34$	High
$7 < t_{cr} \leq 14$	$0.17 \leq S < 0.34$	Moderate-High
$14 < t_{cr} \leq 28$	$0.10 \leq S < 0.17$	Moderate-Low
$t_{cr} > 28$	$S < 0.10$	Low

strength. The lower cracking potential of AAC than OPC based concrete with similar or even lower strength is very positive information for the application of AAC as a building material.

The reason why AAC showed higher autogenous shrinkage but later cracking initiation than OPC based concrete is believed to be mainly due to the stress relaxation. The evident relaxation of AAC is in line with the large creep of AAM paste identified in Ref. [58,59]. These two phenomena, creep and relaxation, both originate from the viscoelasticity of the material [60]. In the next section, the creep part of the autogenous shrinkage will be quantified.

4. Numerical results and discussion

4.1. Calculated stress based on autogenous shrinkage

The calculated stress with Equation (1), based on the autogenous shrinkage (see Fig. 12) and the elastic modulus (see Fig. 11) of the concrete, are presented and compared with measured stress in Fig. 14. It

can be seen that the calculated stress in AAC is around 7–8 times higher than the experimentally measured one. These results confirm that the creep/relaxation plays an important role in the stress development in AAC. The stress is significantly overestimated when the creep part in the autogenous shrinkage and the stress relaxation are not considered.

4.2. Calculated stress based on the elastic part of autogenous shrinkage

According to Equations 2 and 4–6, the elastic part and creep part of the autogenous shrinkage of AAC can be calculated, as shown in Fig. 15.

The calculated stress in AAC according to Equation (3) is shown in Fig. 16. It can be seen that considering only the elastic part of autogenous shrinkage in calculation gives a much better prediction of the shrinkage-induced stress than the results shown in Fig. 14, where the total autogenous shrinkage was used as input. Nonetheless, the calculated stress is still two times higher than the stress measured by TSTM, indicating that the relaxation of the stress has to be considered in order to estimate the time-dependent stress.

4.3. Calculated stress by taking relaxation into account

According to Equations (7)–(9), the stress in AAC by taking relaxation into account is calculated and shown in Fig. 17. It can be seen that the calculation considering the elastic part of the autogenous shrinkage and the relaxation of the stress with time provides a fairly good agreement between calculated and measured stress evolutions in AAC. For AAS concrete, the calculation underestimates the stress in the first 7 days while overestimates the stress at 20 days. For AASF concrete, an opposite trend is observed. This discrepancy is probably because these two concrete mixtures have different creep compliances, but in the calculation, the same model was used.

In Equations (4)–(6), the water-to-solid ratio and the reaction degree were considered for the creep calculation of the paste, however, the creep behaviour of concrete depends not only on the deformability of the paste but also on the restraining effect of the aggregates. The restraining effect of aggregates is determined not only by the size and volume fraction of the aggregates but also by the interface between paste and aggregates, viz. the interfacial transition zone (ITZ) [61,62]. In this study, the size and the volume fraction of aggregates for AAS and AASF concrete are the same (see Table 2), however, differences in the ITZ properties of AAS concrete and AASF concrete were found in previous studies [47,53] which investigated the same mixtures as this study. Generally, AASF concrete has more porous and weaker ITZ than AAS concrete [47,53]. Although the influence of ITZ on the deformation of concrete has not been clearly understood [63–65], it has been found that the creep of the ITZ is higher compared to the bulk matrix [66]. Therefore, the creep compliance of AASF concrete is supposed to be less restrained by the aggregates due to the weaker ITZ. As a result, using the

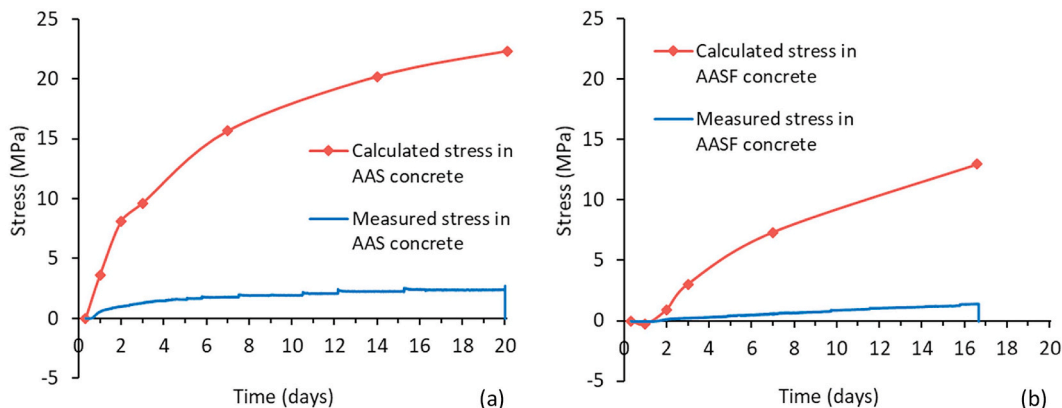


Fig. 14. Calculated stress in AAS (a) and AASF (b) concrete from the autogenous shrinkage and the elastic modulus of the concrete.

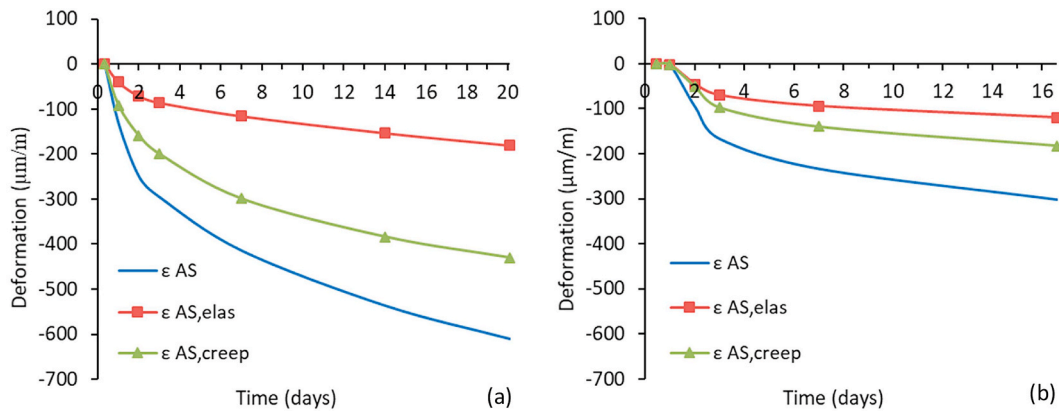


Fig. 15. Calculated elastic part and creep part of autogenous shrinkage of AAS (a) and AASF (b) concrete. The autogenous deformation curve for AASF concrete is modified during modelling in order to exclude the influence of expansion.

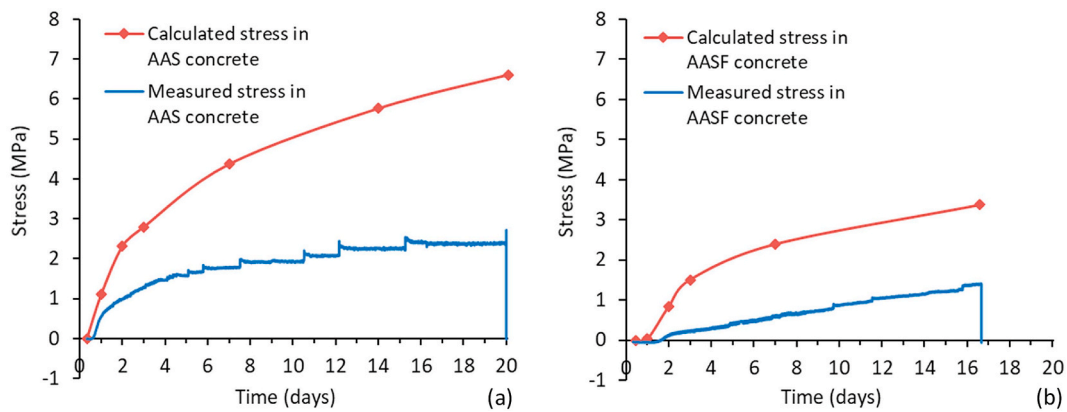


Fig. 16. Calculated stress in AAS (a) and AASF (b) concrete from the elastic part of the autogenous shrinkage and the elastic modulus of the concrete.

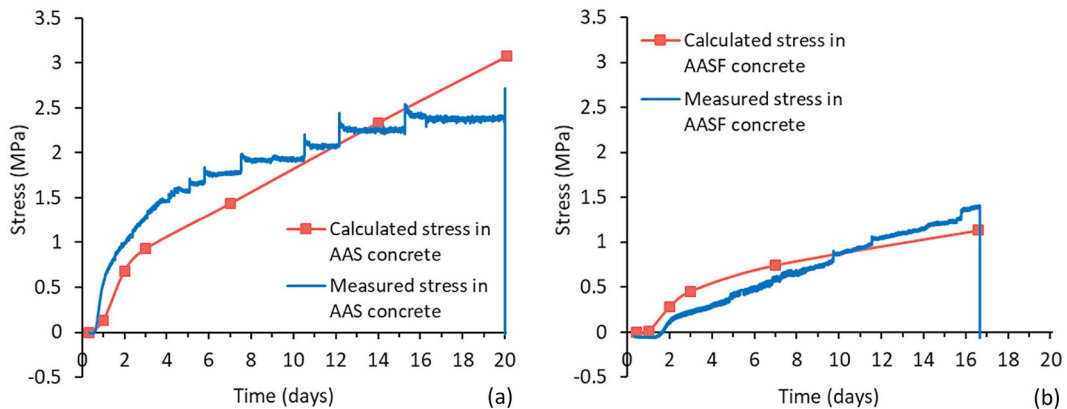


Fig. 17. Calculated stress in AAS (a) and AASF (b) concrete from the elastic part of the autogenous shrinkage and the elastic modulus of the concrete, with the stress relaxation taken into account.

same equations and empirical parameters in calculation may lead to slight overestimation and underestimation of the creep in AAS and AASF concrete, respectively.

Despite the reason for the small discrepancies exhibited in Fig. 17, the calculations in this section have clearly shown the important roles played by relaxation in the stress evolution of restrained AAC. Neglecting the creep and relaxation behaviour would lead to an overestimation of the self-induced stress in AAC.

4.4. Estimation of the cracking initiation of AAC

With the calculated stress and tensile strength, the cracking initiation of the concrete can be estimated. Due to the difficulty in conducting the uniaxial tensile test on concrete, the tensile strength measured by the splitting test on concrete cubes or cylinders is usually used to estimate the cracking potential [67]. However, it should be noted that the maximum stress of concrete at failure is normally lower than the splitting tensile strength. The first reason is that the tensile strength of concrete measured uniaxially is normally lower than the tensile strength

measured by splitting tests [68]. The second reason is the reducing effect of relaxation on the tensile strength. While the relaxation can reduce the stress, it can also aggravate the development of microcracking, which is detrimental to the tensile strength [69,70]. Due to the local creep, viz. change of the internal geometric constitution of the paste, the internal stress is redistributed with time, causing a relief of stress in higher stressed zones but new stress concentration in other zones [34]. As a result, additional local failure within the concrete can be induced. This is probably the reason why the tensile strength of concrete which experiences creep/relaxation under restrained condition is normally lower than that of concrete which is free from loading [69,71]. Therefore, the influence of relaxation on the tensile strength needs also a consideration when estimating the cracking time of the concrete. The third reason is that the cube under splitting stress has to fail in the middle, while the beam under uniaxial tensile stress will fail at the weakest cross-section. Due to the larger size of the beam than the cube, the tensile strength of the weakest cross-section should be statistically lower than that of the middle cross-section of the cube. Hence, a reduced tensile strength is normally considered, as shown in Fig. 18.

For OPC based concrete, the failure stress-to-splitting strength ratios were in the range of 0.7–0.8 [34,72,73]. Based on experiments on a dozen specimens, Lokhorst [34] found OPC based concrete, on average, failed at 75% of the actual tensile splitting strength irrespective of the age. However, the failure stress-to-splitting strength ratios for AAS concrete and AASF concrete in this study were only 0.56 and 0.37, respectively. These ratios were lower than those for OPC concretes, possibly because of the more evident creep/relaxation in AAC. Besides, it should be noted that only a limited number of samples were tested in this study. To obtain a representative reducing factor of the tensile strength of AAC, intensive experimental work on numerous samples and mixtures is needed.

5. Concluding remarks

In this study, the cracking potential of AAS and AASF concrete subjected to restrained autogenous shrinkage is evaluated. Based on the experimental and numerical results, the following remarks can be made:

1. AAC concrete shows generally high compressive strength. The $f_{t,sp}/f_c$ and the elastic modulus of AAC decrease with the curing age, which may be due to the development of microcracking resulting from the continuous autogenous shrinkage.
2. TSTM is utilized for the first time to track the stress evolution and cracking initiation of AAC. AAC is found to show moderate-low cracking potential, despite its high autogenous shrinkage. The low autogenous shrinkage-induced stress in AAC is mainly attributed to the pronounced relaxation of the concrete.

Appendix A

In section 3.4, $Q(t)$ and Q_{max} of AAC was used to calculate the reaction degree and the creep coefficient.

In this study, a TAM Air isothermal calorimeter (Thermometric) was used to measure the reaction heat of the pastes. Before measurements, the calorimeter was calibrated at 20 °C. The temperature of the measuring channels of the calorimeter was controlled at 20 ± 0.01 °C. Approximately 5 g of paste were cast into each glass vial and were immediately loaded into the measuring channels. The internal diameter of the glass vial was 24.5 mm. The mixing and loading procedures lasted about 15min from the moment of adding activator. The data was recorded every 1 min to 7 days. The calorimetry results were normalized by the weight of the paste. The heat flow of the paste is shown in Fig. A.1 (a) and the $Q(t)$ of AAS and AASF pastes during the first week of reaction was shown in Fig. A.1 (b). Due to the same curing condition (iso-thermal) of the paste and concrete samples, the reaction degrees of the paste and the concrete are assumed identical at all time.

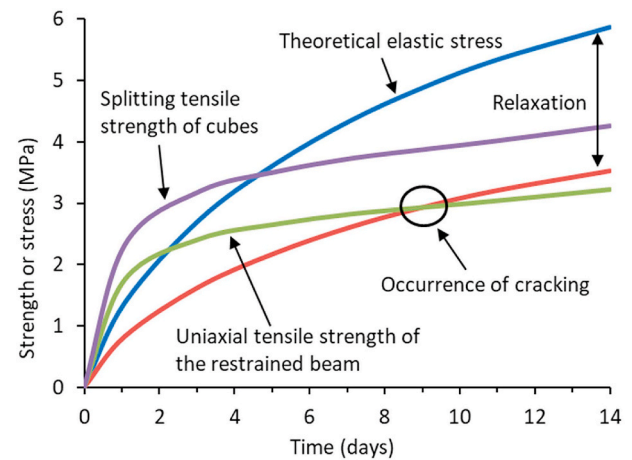


Fig. 18. A schematic diagram of the stress development and the resultant cracking of concrete due to restrained shrinkage.

3. With the elastic part of the autogenous shrinkage and the stress relaxation taken into account, a very good prediction of the stress evolution in AAC is obtained. In contrast, calculations without considering the creep and relaxation would lead to a significant overestimation of the stress in AAC.
4. A reducing factor of the splitting tensile strength should be considered when estimating the cracking time of restrained AAC, since the failure stress of the restrained beam is lower than the splitting tensile strength of cubes that are free from load during curing.

Declaration of competing interest

The authors declare that they have no known competing financial interests or personal relationships that could have appeared to influence the work reported in this paper.

Acknowledgment

Zhenming Li and Xuhui Liang would like to acknowledge the funding supported by the China Scholarship Council (CSC) under grant No. 201506120072 and No. 201806050051. This work is supported also by the grant from the Netherlands Organisation for Scientific Research (NWO). Prof. Klaas van Breugel is acknowledged for the discussion on the model. The two anonymous reviewers are appreciated for their few but valuable comments.

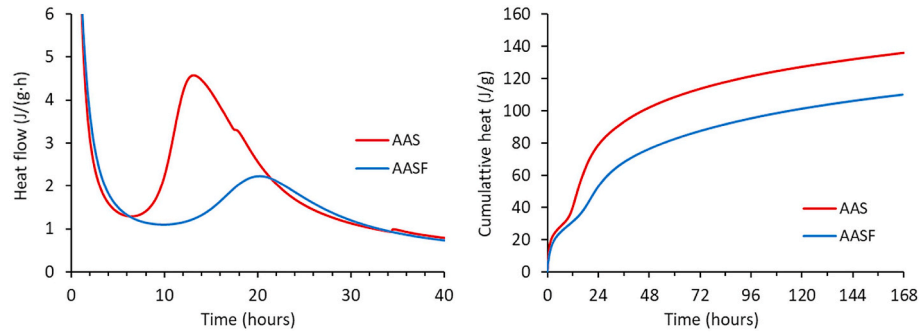


Fig.A.1. Reaction heat of AAS and AASF pastes.

For the $Q(t)$ after the first week and the Q_{max} of the paste/concrete, the method of curve fitting is needed. According to Ref. [43,74,75], the exponential model shown in Equation (A.1) can provide a good Q_{max} prediction for AAMs.

$$Q(t) = Q_{max} \exp \left[- \left(\frac{\tau}{t} \right)^\beta \right] \quad (\text{A.1})$$

where τ and β are the fitting parameters associated with the time and the shape of the exponential model.

Due to the inability of Equation A.1 to fit multi-curvature evolutions, a piecewise approximation by two functions is needed for the fitting of the heat flow curves of AAMs paste. The fitted curves of the heat flow of AAS and AASF pastes are presented in Fig. A.2, in comparison with the experimental data. The fitting parameters and the accuracy of the fitting (indicated by the adjusted R-square) are shown in Table A.1.

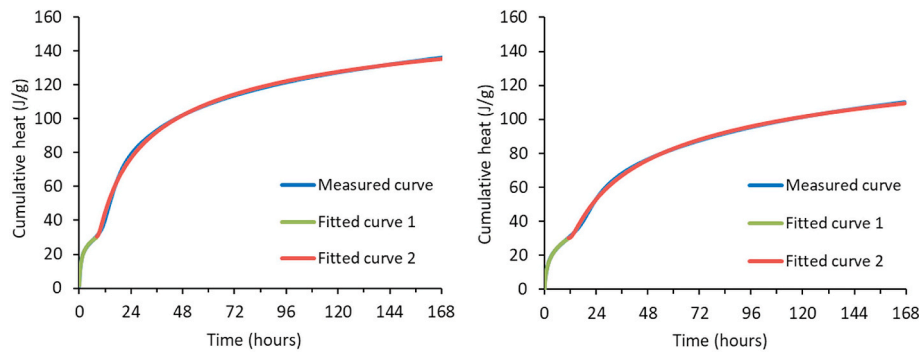


Fig. A.2. Fitted heat flow of AAS paste (a) and AASF paste (b), in comparison with the experimentally measured heat flow.

Table A.1

Fitted parameters of the exponential model for the heat flow of AAS and AASF paste.

Mixtures	Q_{max}	τ	β	R-square
AAS curve 1	–	1.98	0.33	0.998
AAS curve 2	155.04	23.68	0.49	0.998
AASF curve 1	–	44.02	0.22	0.999
AASF curve 2	139.13	46.04	0.47	0.999

Fig. A.2 and Table A.1 indicate a very good fitting of the curves. It can be seen in Table A.1 that AAS paste has a higher Q_{max} than AASF paste, which is reasonable. With the fitted parameters, the $Q(t)$ and the reaction degree α of AAS and AASF concrete at different curing ages can be then calculated, as shown in Table A.2. The results were used to in section 3.4 to calculate the creep coefficient.

Table A.2

$Q(t)$ and α of AAS and AASF concrete at different ages.

AAS concrete	8h	1d	2d	3d	7d	14d	20d
$Q(t)$	30.53	78.90	102.09	113.70	135.98	148.63	153.70
α	0.20	0.51	0.66	0.73	0.88	0.96	0.99
AASF concrete	11h	1d	2d	3d	7d	16.6d	–
$Q(t)$	29.77	53.67	77.03	88.11	110.65	127.00	–
α	0.19	0.39	0.55	0.63	0.80	0.91	–

References

- [1] G. Habert, C. Ouellet-Plamondon, Recent update on the environmental impact of geopolymers, *RILEM Tech. Lett.* 1 (2016) 17–23.
- [2] J.L. Provis, S.A. Bernal, Geopolymers and related alkali-activated materials, *Annu. Rev. Mater. Res.* 44 (2014) 299–327, <https://doi.org/10.1146/annurev-matsci-070813-113515>.
- [3] J.L. Provis, Alkali-activated materials, *Cement Concr. Res.* 114 (2018) 40–48, <https://doi.org/10.1016/j.cemconres.2017.02.009>.
- [4] C. Shi, A.F. Jiménez, A. Palomo, New cements for the 21st century: the pursuit of an alternative to Portland cement, *Cement Concr. Res.* 41 (2011) 750–763, <https://doi.org/10.1016/j.cemconres.2011.03.016>.
- [5] ASTM C618 - 19, Standard Specification for Coal Fly Ash and Raw or Calcined Natural Pozzolan for Use in Concrete, 2008, <https://doi.org/10.1520/C0618-19.2>.
- [6] N. Gamage, K. Liyanage, S. Fragomeni, S. Setunge, Overview of Different Types of Fly Ash and Their Use as a Building and Construction Material, 2013.
- [7] J.L. Provis, Activating solution chemistry for geopolymers, in: *Geopolymers*, Elsevier, 2009, pp. 50–71.
- [8] F. Collins, J.G. Sanjayan, Early age strength and workability of slag pastes activated by NaOH and Na₂CO₃, *Cement Concr. Res.* 28 (1998) 655–664.
- [9] H. Tan, X. Deng, X. He, J. Zhang, X. Zhang, Y. Su, J. Yang, Compressive strength and hydration process of wet-grinded granulated blast-furnace slag activated by sodium sulfate and sodium carbonate, *Cement Concr. Compos.* 97 (2019) 387–398, <https://doi.org/10.1016/j.cemconcomp.2019.01.012>.
- [10] J.L. Provis, J.S.J. Van Deventer, Alkali Activated Materials, 2014, <https://doi.org/10.1007/978-94-007-7672-2>.
- [11] B.S. Gebregziabihier, R.J. Thomas, S. Peethamparan, Temperature and activator effect on early-age reaction kinetics of alkali-activated slag binders, *Construct. Build. Mater.* 113 (2016) 783–793, <https://doi.org/10.1016/j.conbuildmat.2016.03.098>.
- [12] M. Ben Haha, G. Le Saout, F. Winnefeld, B. Lothenbach, Influence of activator type on hydration kinetics, hydrate assemblage and microstructural development of alkali activated blast-furnace slags, *Cement Concr. Res.* 41 (2011) 301–310, <https://doi.org/10.1016/j.cemconres.2010.11.016>.
- [13] F. Pacheco-Torgal, Z. Abdollahnejad, S. Miraldo, M. Kheradmand, Alkali-activated Cement-Based Binders (AACBs) as Durable and Cost-Competitive low-CO₂ Binder Materials: Some Shortcomings that Need to Be Addressed, *Butterworth-Heinemann*, Oxford, UK, 2017.
- [14] F. Pacheco-Torgal, Z. Abdollahnejad, A.F. Camões, M. Jamshidi, Y. Ding, Durability of alkali-activated binders: a clear advantage over Portland cement or an unproven issue? *Construct. Build. Mater.* 30 (2012) 400–405, <https://doi.org/10.1016/j.conbuildmat.2011.12.017>.
- [15] M. Mastali, P. Kinnunen, A. Dalvand, R. Mohammadi Firouz, M. Ilkainen, Drying shrinkage in alkali-activated binders – a critical review, *Construct. Build. Mater.* 190 (2018) 533–550, <https://doi.org/10.1016/j.conbuildmat.2018.09.125>.
- [16] J. Ma, F. Dehn, Shrinkage and creep behavior of an alkali-activated slag concrete, *Struct. Concr.* 18 (2017) 801–810, <https://doi.org/10.1002/suco.201600147>.
- [17] C. Cartwright, F. Rajabipour, A. Radli, Shrinkage characteristics of alkali-activated slag cements, *J. Mater. Civ. Eng.* 27 (2014) 1–9, [https://doi.org/10.1061/\(ASCE\)MT.1943-5533.0001058](https://doi.org/10.1061/(ASCE)MT.1943-5533.0001058).
- [18] B.D. Kumarappa, S. Peethamparan, M. Ngami, Autogenous shrinkage of alkali activated slag mortars: basic mechanisms and mitigation methods, *Cement Concr. Res.* 109 (2018) 1–9, <https://doi.org/10.1016/j.cemconres.2018.04.004>.
- [19] S. Uppalapati, Ö. Cizer, Assessing the Autogenous Shrinkage of Alkali-Activated Slag/Fly Ash Mortar Blends, *Am. Concr. Institute, ACI Spec.* 2017, Publ. 2017-Janua.
- [20] G. Fang, W. Tu, Y. Zhu, M. Zhang, Autogenous shrinkage of alkali-activated fly ash slag pastes with and without SAP, in: *4th Int. Conf. Serv. Life Des. Infrastructures*, 2018, pp. 449–455.
- [21] M. Nedeljković, Z. Li, G. Ye, Setting, strength, and autogenous shrinkage of alkali-activated fly ash and slag pastes: effect of slag content, *Materials (Basel)* 11 (2018) 2121, <https://doi.org/10.3390/ma11112121>.
- [22] Z. Li, S. Zhang, X. Liang, G. Ye, Internal curing of alkali-activated slag-fly ash paste with superabsorbent polymers, *Construct. Build. Mater.* (2020) (under review).
- [23] Z. Li, M. Wyrzykowski, H. Dong, J. Granja, M. Azenha, P. Lura, G. Ye, Internal curing by superabsorbent polymers in alkali-activated slag, *Cement Concr. Res.* 135 (2020) 106123, <https://doi.org/10.1016/j.cemconres.2020.106123>.
- [24] Z. Li, M. Nedeljković, Y. Zuo, G. Ye, Autogenous shrinkage of alkali-activated slag-fly ash pastes, in: *5th Int. Slag Valoriz. Symp.*, Leuven, 2017, pp. 369–372.
- [25] A.M. Neville, Properties of Concrete, 2011.
- [26] E. Tazawa, Autogenous Shrinkage of Concrete, CRC Press, 1998.
- [27] M.S. Sule, Effect of Reinforcement on Early-Age Cracking in High Strength Concrete, Delft University of Technology, 2003.
- [28] P. Lura, Autogenous Deformation and Internal Curing of Concrete, Delft University of Technology, 2003.
- [29] Z. Li, A. Kostuchenko, G. Ye, Autogenous shrinkage-induced stress of alkali-activated slag and fly ash concrete under restraint condition, in: *ECI (Ed.), Alkali Act. Mater. Geopolymers Versatile Mater. Offer. High Perform. Low Emiss.*, Tomar, 2018, p. 24.
- [30] S.I. Igarashi, A. Bentur, K. Kovler, Autogenous shrinkage and induced restraining stresses in high-strength concretes, *Cement Concr. Res.* 30 (2000) 1701–1707, [https://doi.org/10.1016/S0008-8846\(00\)00399-9](https://doi.org/10.1016/S0008-8846(00)00399-9).
- [31] F. Collins, J.G. Sanjayan, Cracking tendency of alkali-activated slag concrete subjected to restrained shrinkage, *Cement Concr. Res.* 30 (2000) 791–798, [https://doi.org/10.1016/S0008-8846\(00\)00243-X](https://doi.org/10.1016/S0008-8846(00)00243-X).
- [32] NEN-EN 12390-3, Testing Hardened Concrete - Part 3: Compressive Strength of Test Specimens, 2009.
- [33] B. Delsaute, C. Boulay, J. Granja, J. Carette, M. Azenha, C. Dumoulin, G. Karaïskos, A. Deraemaeker, S. Staquet, Testing concrete E-modulus at very early ages through several techniques: an inter-laboratory comparison, *Strain* (2016) 91–109, <https://doi.org/10.1111/str.12172>.
- [34] S.J. Lokhorst, Deformational Behaviour of Concrete Influenced by Hydration Related Changes of the Microstructure, Delft University of Technology, 2001.
- [35] ASTM C 1581, Standard Test Method for Determining Age at Cracking and Induced Tensile Stress Characteristics of Mortar and Concrete under Restrained Shrinkage, ASTM Int., 2009, pp. 1–7, <https://doi.org/10.1520/C1581>.
- [36] Z. Li, T. Lu, X. Liang, H. Dong, J. Granja, M. Azenha, G. Ye, Mechanisms of autogenous shrinkage of alkali-activated slag and fly ash pastes, *Cement Concr. Res.* 135 (2020) 106107, <https://doi.org/10.1016/j.cemconres.2020.106107>.
- [37] T. Lu, Autogenous Shrinkage of Early Age Cement Paste and Mortar, Delft University of Technology, 2019.
- [38] K. Van Breugel, Relaxation of Young Concrete, 1980, p. 144.
- [39] Z.P. Bazant, Prediction of concrete creep effects using age-adjusted effective modulus method, *J. Am. Concr. Inst.* 69 (1972) 212–217.
- [40] H. van der Ham, E. Koenders, K. van Breugel, Creep model uncertainties in early-age concrete simulations, *Proc. Concreep.* 8 (2008) 431–436.
- [41] K.A. Riding, J.L. Poole, K.J. Folliard, M.C.G. Juenger, A.K. Schindler, Modeling hydration of cementitious systems, *ACI Mater. J.* 109 (2012) 225–234.
- [42] A.K. Schindler, K.J. Folliard, Heat of hydration models for cementitious materials, *ACI Mater. J.* 102 (2005) 24.
- [43] D. Ravikumar, N. Neithalath, Reaction kinetics in sodium silicate powder and liquid activated slag binders evaluated using isothermal calorimetry, *Thermochim. Acta* 546 (2012) 32–43, <https://doi.org/10.1016/j.tca.2012.07.010>.
- [44] F. Wittmann, Bestimmung physikalischer Eigenschaften des Zementsteins, 1974.
- [45] NEN-EN 206-1, Concrete - Part 1: specification, performance, production and conformity, Eur. Comm. Stand. (2001).
- [46] A. Fernández-Jiménez, J.G. Palomo, F. Puertas, Alkali-activated slag mortars: mechanical strength behaviour, *Cement Concr. Res.* 29 (1999) 1313–1321.
- [47] M. Nedeljković, Carbonation Mechanism of Alkali-Activated Fly Ash and Slag Materials: in View of Long-Term Performance Predictions, Delft University of Technology, 2019.
- [48] F. Puertas, S. Martínez-Ramírez, S. Alonso, T. Vázquez, Alkali-activated fly ash/slag cements. Strength behaviour and hydration products, *Cement Concr. Res.* 30 (2000) 1625–1632, [https://doi.org/10.1016/S0008-8846\(00\)00298-2](https://doi.org/10.1016/S0008-8846(00)00298-2).
- [49] Y. Ma, Microstructure and Engineering Properties of Alkali Activated Fly Ash - as an Environment Friendly Alternative to Portland Cement, 2013.
- [50] Z. Yu, Microstructure Development and Transport Properties of Portland Cement-Fly Ash Binary Systems, 2015.
- [51] N. Arioglu, Z. Canan Girgin, E. Arioglu, Evaluation of ratio between splitting tensile strength and compressive strength for concretes up to 120 MPa and its application in strength criterion, *ACI Mater. J.* 103 (2006) 18–24, <https://doi.org/10.14359/15123>.
- [52] Z. Li, M. Nedeljković, B. Chen, G. Ye, Mitigating the autogenous shrinkage of alkali-activated slag by metakaolin, *Cement Concr. Res.* 122 (2019) 30–41, <https://doi.org/10.1016/j.cemconres.2019.04.016>.
- [53] S. Prinsse, D.A. Hordijk, G. Ye, P. Legendijk, M. Luković, Time-dependent material properties and reinforced beams behavior of two alkali-activated types of concrete, *Struct. Concr.* 21 (2020) 642–658, <https://doi.org/10.1002/suco.201900235>.
- [54] P. Lura, O.M. Jensen, J. Weiss, Cracking in cement paste induced by autogenous shrinkage, *Mater. Struct.* 42 (2009) 1089–1099, <https://doi.org/10.1617/s11527-008-9445-z>.
- [55] F. Collins, J.G. Sanjayan, Microcracking and strength development of alkali activated slag concrete, *Cement Concr. Compos.* 23 (2001) 345–352, [https://doi.org/10.1016/S0958-9465\(01\)00003-8](https://doi.org/10.1016/S0958-9465(01)00003-8).
- [56] P. Lura, K. Van Breugel, I. Maruyama, Effect of curing temperature and type of cement on early-age shrinkage of high-performance concrete, *Cement Concr. Res.* 31 (2001) 1867–1872, [https://doi.org/10.1016/S0008-8846\(01\)00601-9](https://doi.org/10.1016/S0008-8846(01)00601-9).
- [57] A. Darquennes, S. Staquet, M.P. Delplancke-Ogletree, B. Espion, Effect of autogenous deformation on the cracking risk of slag cement concretes, *Cement Concr. Compos.* 33 (2011) 368–379, <https://doi.org/10.1016/j.cemconcomp.2010.12.003>.
- [58] H. Ye, A. Radlińska, Shrinkage mechanisms of alkali-activated slag, *Cement Concr. Res.* 88 (2016) 126–135, <https://doi.org/10.1016/j.cemconres.2016.07.001>.
- [59] A. Kostuchenko, J. Liu, Z. Aldin, Mechanical properties and creep behavior of an alkali-activated concretemechanical properties and creep behavior of an alkali-activated concrete, in: *Alkali Act. Mater. Geopolymers Versatile Mater. Offer. High Perform. Low Emiss.*, 2018, p. 9.
- [60] T.C. Hansen, Creep and Stress Relaxation of Concrete: a Theoretical and Experimental Investigation, Svenska Forskningsinstitutet För Cement Och Betong Vid Kungl. Tekniska högskolan, 1960.
- [61] R.L. Al-Mufti, A.N. Fried, Pulse velocity assessment of early age creep of concrete, *Construct. Build. Mater.* 121 (2016) 622–628.
- [62] O. Bernard, F.-J. Ulm, J.T. Germaine, Volume and deviator creep of calcium-leached cement-based materials, *Cement Concr. Res.* 33 (2003) 1127–1136.
- [63] M. Briffaut, F. Benboudjema, C. Laborde, J.-M. Torrenti, Creep consideration effect on meso-scale modeling of concrete hydration process and consequences on the mechanical behavior, *J. Eng. Mech.* 139 (2013) 1808–1817.
- [64] C. Pichler, R. Lackner, A multiscale creep model as basis for simulation of early-age concrete behavior, *Comput. Concr.* 5 (2008) 295–328.

- [65] P. Lura, M. Wyrzykowski, Influence of aggregate restraint on volume changes: experiments and modelling, in: *Concreep*, 2015, pp. 17–23, <https://doi.org/10.1061/9780784479346>.
- [66] V. Zacharda, J. Němeček, H. Šimonová, B. Kucharczyková, M. Vyhlídal, Z. Keršner, Influence of interfacial transition zone on local and overall fracture response of cementitious composites, in: *Key Eng. Mater.*, 2018, pp. 97–102.
- [67] NEN-EN 12390-3, Testing Hardened Concrete - Part 6: Tensile Splitting Strength of Test Specimens, 2009.
- [68] British Standards Institution, Eurocode 2: Design of Concrete Structures: Part 1-1: General Rules and Rules for Buildings, British Standards Institution, 2004.
- [69] D.J. Cook, P. Chindaprasirt, Influence of loading history upon the tensile properties of concrete, *Mag. Concr. Res.* 33 (1981) 154–160, <https://doi.org/10.1680/mac.1981.33.116.154>.
- [70] A.D. Ross, Creep of concrete under variable stress, *J. Proc.* (1958) 739–758.
- [71] D.J. Cook, P. Chindaprasirt, Influence of loading history upon the compressive properties of concrete, *Mag. Concr. Res.* 32 (1980) 89–100.
- [72] H.G. Heilmann, H. Hilsdorf, K. Finsterwalder, Strength and deformation of concrete under tensile stress, *Bulletin* (1969) 94.
- [73] J. Byfors, Plain Concrete at Early Ages, *Cement-och betonginst.*, 1980.
- [74] S. Chithiraputhiran, N. Neithalath, Isothermal reaction kinetics and temperature dependence of alkali activation of slag, fly ash and their blends, *Construct. Build. Mater.* 45 (2013) 233–242, <https://doi.org/10.1016/j.conbuildmat.2013.03.061>.
- [75] S. Zhang, Y. Zuo, Z. Li, G. Ye, Isothermal calorimetric study on heat evolution and apparent activation energy of alkali-activated slag/fly ash paste, in: *2nd Int. Conf. Sustain. Build. Mater.*, Eindhoven, 2019, pp. 1–8.
- [76] Tianshi Lu, Zhenming Li, Effect of Supplementary Materials on the Autogenous Shrinkage of Cement Paste, *Materials* 13 (15) (2020) 3367.